Spall strength dependence on grain size and strain rate in tantalum

T.P. Remington[a], E.N. Hahn[a,b], S. Zhao[a], R. Flanagan[a], J.C.E. Mertens[c], S. Sabbaghianrad[d], T.G. Langdon[d], C.E. Wehrenberg[e], B.R. Maddox[e], D.C. Swift[e], B.A. Remington[e], N. Chawla[c], M.A. Meyers[a]

[a]*University of California San Diego, La Jolla, CA 92093, USA*
[b]*Los Alamos National Laboratory, Los Alamos, NM 87544, USA*
[c]*Arizona State University, Tempe, AZ 85287, USA*
[d]*University of Southern California, Los Angeles, CA 90089, USA*
[e]*Lawrence Livermore National Laboratory, Livermore, CA 94550, USA*

Abstract

We examine the effect of grain size on the dynamic failure tantalum during laser-shock compression and release and identify a significant effect of grain size on spall strength, which is opposite the prediction of the Hall-Petch relationship: monocrystals have a higher spall strength than polycrystals, which, in turn, are stronger in tension than ultrafine grain sized specimens. Post-shock characterization reveals ductile failure which evolves by void nucleation, growth, and coalescence. Whereas in the monocrystal the voids grow in the interior, nucleation is both intra and intergranular in the poly and UFG crystals. The fact that spall is primarily intergranular in both poly and nanocrystalline samples is strong evidence for higher growth rates of intergranular voids, which have a distinctly oblate spheroid shape in contrast with intragranular voids, which are more spherical. Consistent with prior literature and theory we also identify an increase with spall strength with strain rate from $6x10^6$ to $5x10^7$ s^{-1}. Molecular dynamics calculations agree with the experimental results and also predict grain-boundary separation in the spalling of polycrystals as well as an increase in spall strength with strain rate. An analytical model based on the kinetics of nucleation and growth of intra and intergranular voids and extending the

Keywords: spall strength; strain rate; grain size; texture; void growth

Curran-Seaman-Shockey theory is applied which shows the competition between the two processes for polycrystals.

1. Introduction

Spalling, the failure of matter by tensile pulses resulting from the interaction of stress waves, is of interest for a wide range of applications including ballistic impact, dynamic fragmentation in hypervelocity particle-target interactions, and optical and/or diagnostic equipment hazards inside laser chambers[1–4]. The phenomenon of dynamic failure by spallation is well known and has been reviewed by in a number of contributions[4–7]. There have been extensive studies using the flyer-plate method to determine spall strength and the corresponding mechanisms of failure in face-centered cubic (fcc) metals. Studies of spallation in body-centered cubic (bcc) metals using laser-driven shock have more recently gained momentum, but much space remains for systematic studies at large strain rates and varying initial microstructure[8–14]. Presented herein are the results of an investigation on the effects of grain size and strain rate on the spall strength of tantalum, a model bcc metal. Specifically, the experiments were designed to evaluate differences in spall strength between single, poly, and nano crystalline Ta at the extreme strain rates enabled by laser shock pulses. Of particular importance is the identification of the nucleation sites and the evolution of damage leading to spalling. The experimental results are complemented by molecular dynamics simulation and an analysis based on the Seaman-Shockey-Curran theory [15–17].

When a laser pulse irradiates the surface of a specimen, a high temperature and pressure plasma are formed. The rapidly expanding plasma induces a shock wave via the rocket effect; the

shock wave travels through the specimen until reaching the rear free surface of the sample where release (rarefaction) waves are generated due to free surface boundary conditions. The interaction of the release (rarefaction) waves generates tensile stresses within the sample. If the tensile pulse exceeds a critical threshold stress of the sample, the material undergoes dynamic failure, known as spalling [18–22]. Laser shock in combination with VISAR measurements has been successfully used to determine the spall strength of metals in the 0.1-10 ns time ranges.

Previous spall strength measurements of single and polycrystalline tantalum show a potential grain size effect by comparing single and polycrystalline samples [23]. So far there have been no comprehensive studies comparing single, poly and nanocrystalline tantalum spall strengths. Furthermore, there is limited experimental spall strength data for tantalum for ultrathin samples at strain rates above 10^6 s^{-1}. Recent works attempt to remedy this dearth of information [23–26].

In this work we aim to (1) compare the spall strengths of single, poly and nanocrystalline Ta laser shocked under the same conditions; (2) establish the effect of strain rate on spall strength; and (3) develop a mechanistic understanding of the processes involved in the tensile failure.

2. Experimental Methods

2.1. Materials and Characterization

Monocrystalline tantalum samples were purchased from Marketech and polycrystalline Ta samples were acquired through the Lawrence Livermore National Laboratory (LLNL) national stock. The grain size of the polycrystal was measured under SEM observation to be ~20 μm. Nanocrystalline Ta samples were produced from the polycrystalline samples using high-pressure torsion (HPT) processing as previously described [27]. The HPT was conducted under

quasi-constrained conditions [28] and produced an average grain size of ~100 nm in the shock direction. An earlier report described the first comprehensive processing of Ta by HPT [29].

X-ray micro-CT was used to study fully contained spall voiding volumetrically and non-destructively. X-ray transmission microtomography was performed using a custom lab-scale instrument [30,31]. This system provided high X-ray energy for dense metal imaging and imaging resolution suitable to the study of microstructural features.

2.2 Experimental Design

Nano, poly, and monocrystalline tantalum samples were cut by a low-speed diamond saw and mechanically polished to 250 μm and 50 μm thickness. Samples were assembled by The Schafer Corporation, Livermore, CA using adhesive to attach a 20 μm thick polystyrene ablator to one side. All glue was tacked on to the edges of the samples in order to minimize the gap between the polystyrene and sample surface. The polystyrene layer acts as a heat shield for the tantalum samples and protects them against direct ablation and hot spots inherent in the laser energy profile. The experimental setup is displayed in Figure 1. Recovery of laser shocked samples ranging from incipient to complete spall was enabled by an aerogel that decelerated and caught the specimens in a recovery tube, Fig. 1(a).

1-D radiation-hydrodynamic simulations (run using HYADES [32]) guided the experimental parameters of the laser energy, pulse shape, pulse duration, and sample thickness. Samples were laser shocked in the Janus laser chamber (a component of the Jupiter Laser Facility at Lawrence Livermore National Laboratory). Spall was generated in the mono, poly, and nanocrystalline Ta samples by laser shocking all the samples at the same laser energy, 100 J, and sample thickness, 250 μm. HYDAES simulations showed an increase in strain rate when sample thickness was reduced from 250 to 50 μm. Single and nanocrystalline Ta samples with

50 μm thickness were laser shocked at 75 and 100 J energy to test spall strength dependence on strain rate.

The velocity history of the free rear surface of the samples was recorded using VISAR [33], Fig. 1(e). Data were collected for each laser shocked sample and processed to obtain the free surface velocity versus time profiles from which the spall strengths, peak pressures, and strain rates were extracted.

2.3 Micro-Computed Tomography

Using micro-CT, 3-D images of the voids in an incipient spall bubble were obtained for polycrystalline tantalum samples. A 250 μm thick disk exhibiting a spall bubble was cut down to remove material around the bubble zone (~1 mm diameter) before conducting micro-CT scanning in order to improve the transmitted X-ray signal. The cut sample had a maximum width of ~800 μm. The sample was seated on the micro-CT rotation stage using adhesive and mounted to a 1/8 inch aluminum post. X-ray imaging was conducted at 140 kV and 40 μA target current using a reflection style tungsten target and the custom X-ray detector. X-ray projections were acquired in 512^2 pixel format at unique and periodic 0.5° increments over a 180° range. The distance from the X-ray spot to the sample was roughly 7.5 mm and an X-ray magnification factor of 9.76x was used. Reconstructions were performed using a fast Fourier transform MATLAB implementation of the Feldkamp-Davis-Kress filtered back projection cone-beam tomography algorithm and Hann filter. The effective voxel size in the reconstruction volume was 1.96 μm.

2.4. Spall Strength Calculation

The acoustic approximation simplifies the integrated equations of motion by considering the shock and release waves weak so that their velocities are approximated as the sound velocity [34]. The acoustic approximation is:

$$P_{spall} = (1/2)\rho_0 c(u_{max} - u_{min}), \quad (1)$$

where ρ_0 is the initial density of the material, c is the sound velocity, u_{max} is the peak velocity of the free rear surface (shock breakout), and u_{min} is the first minimum velocity (spall pull-back) [35,36].

Figure 2 shows free surface velocity traces of an ideal ductile spall curve[34], flyer plate [37], laser driven system, and molecular dynamics simulation[14] with excellent qualitative agreement across methods. We employ molecular dynamics simulations to visualize the internal stress states and void development relative to a free surface velocity trace for illustrative purposes. The simulation was carried out for a single crystal sample using LAMMPS [38] and employed an interatomic potential developed for tantalum under shock conditions by Ravelo et al. [39]. Details of the methodology are provided in previous literature [13,14]. Points 1-5 correspond to the molecular dynamics curve in Fig. 2(d). Point 1 indicates the stationary free surface while the compressive wave traverses the sample. Point 2 indicates the rapid shock rise shortly after the arrival of the shock wave, and right below this point is the typical kink indicative of the Hugoniot elastic limit. Point 3 corresponds to the maximum rear surface velocity, u_{max}, and marks the start of relaxation[40] – the rarefaction wave begins returning into the sample at the beginning of the preceding plateau and for short pulse durations, the width of the plateau approaches zero. Point 4 is the material undergoing tension at the spall plane. Point 5 is the arrival of the plastic release wave at the rear surface and marks the minimum rear surface velocity, u_{min} [41]. Figure 2e qualitatively illustrates the material response at characteristic times

during spallation in tantalum. All of the present microscopy is conducted post-mortem - many challenges exist in correlating the final microstructure to the different stages of the dynamic spall process.

The strain rates were calculated by applying a classical acoustic approximation:

$$\dot{\varepsilon} = (u_{max} - u_{min})/(\Delta t \times 2c) \quad (2)$$

where Δt is the time difference between $u_{\max}$ and $u_{\min}$ from the VISAR plot. The experiments used two specimen thicknesses, 250 and 50 μm, and yielded strain rates of approximately $6x10^6$ and $5x10^7$ s^{-1}, respectively. By reducing the sample thickness the strain rate is increased by a factor of ten.

3. Results

Spalled samples were characterized by SEM and micro-CT scans to identify the mechanisms of failure. SEM images of single, poly and nanocrystalline Ta show dimpling on the surfaces which strongly suggests that tantalum spalled by ductile failure (Fig. 3). Monocrystalline tantalum failed by the nucleation, growth and coalescence of voids at the spall plane, Fig. 3(a-c). Voids may grow from any inclusions or impurities in the metal. Conversely, both poly and nano crystalline Ta were observed to have substantial intergranular voiding. This is clearly seen in the relatively coarse-grained polycrystalline material, Fig. 3(d-f).

3.1 Micro-Computed Tomography

Micro-CT reconstructed images of a plane sectioning the spall bubble, perpendicular to the rotation axis of the scan, are provided in Figure 4. Bright light phases correspond to those which are highly attenuating (tantalum) and the dark phases correspond to those which are lowly attenuating (air/voids). Several reconstruction artifacts present in the dataset can be seen in Figure 4. The brightening of the periphery, or the darkening of the interior, is known as beam-

hardening induced intensity cupping and is a result of the polychromatic X-ray beam used for attenuation imaging.[42,43] Also, ring-like artifacts are observed, which are essentially the result of sensor miscalibration or beam instability[44]. In addition to the spall bubble volume itself, nodular features at the interior of the void's surface are observed. The nominal size of these features is comparable to the grain size observed via SEM (Fig. 3(e)), indicating that the tortuous surface is principally attributed to grain-boundary separation and demonstrates that the grain boundaries are weaker, at the imposed strain rates, than the bulk material. The spalled area has a square shape, which is due to the phase plate used to homogenize the laser energy distribution. The dimension of the phase plate is 1 mm^2, which approximately corresponds to the diameter of the spall.

A virtual cross section of the sample near the edge of the bubble feature is provided in Figure 4(c), where the nodules of the opposing sides appear to have at one point been continuous. The selective separation of certain grain boundaries re-emphasizes that microstructure plays an important role in the failure of tantalum. Figure 4(d) contains a cross section near the center of the bubble, where one particularly large nodule (grain) can be seen to correspond with a dimple of similar size on the opposing surface, quite probably where the grain was positioned prior to spalling. The spall bubble was also observed to be bound at the periphery through grains acting as branching ligaments in the spall plane, as shown in Figure 7(b) (intact ligaments can be seen).

Micro-CT images also revealed microvoids in the spall zone of polycrystalline tantalum. Figure 4(e-g) are provided to demonstrate the 3-D information contained within the CT dataset, wherein artificial sections are taken through the dataset at decreasing proximity from the spall

bubble. Similar to the SEM observations, micro-CT imaging indicated intergranular voiding mechanisms that were active in the spalling of granular tantalum.

In order to characterize the spall failure using X-ray micro-CT, the 2-D slices of tantalum had to be segmented. A non-local means (NLM) filtering followed by a simple threshold was used to obtain the segmented images. NLM filtering and segmented volume rendering were performed in Avizo Fire (FEI). The segmented volume offered more manageable interpretation, quantification, and visualization than the grayscale volume. Figures 4(a-b) contain renderings of the segmented 3-D volume derived from micro-CT imaging of the polycrystalline tantalum sample subjected to spall conditions. The rough spall surface indicates that a large quantity of free surface area was created during separation.

3.2 Microstructural Characterization in the Vicinity of the Spall Plane

To understand the influence of the microstructure on the dynamic failure of tantalum, scanning electron microscopy (SEM) and electron backscattered diffraction (EBSD) characterization was performed on the cross section of the as-shocked monocrystalline (Fig. 5), coarse grained polycrystalline (Fig. 6), as well as ultrafine grained specimen (Fig. 7). For the monocrystalline sample, profuse voids have been identified in the vicinity of the spall plane. Molecular dynamics simulation by Traiviratana et al. [45] revealed (their Fig. 8), albeit at a much smaller scale, geometrical facets acquired by void formation in copper. In fcc metals, voids have been observed to have faceted sides by virtue of the anisotropy of flow stress [5]. However, the present results do not show this deviation from sphericity because the size of the voids is near the resolution limit of the present EBSD analysis.

For polycrystalline materials, as shown in Fig. 6 and Fig. 7, the density of voids seems to be higher than that of the monocrystalline sample. EBSD mapping suggests that these voids are

preferentially located at the grain boundaries, although some of them can be found in the grain interior as well. The fact that the fracture is primarily intergranular suggest that voids nucleate in greater proportion at the grain boundaries and grow faster at these locations.

3.3 Measurement of Spall Strength

Figure 8 shows the velocity versus time profile for monocrystalline tantalum samples of varying thickness. Each sample has two curves corresponding to two VISAR traces. The degree to which they are in sync indicates that the data is conclusive and appropriately calibrated to each other and the experimental parameters. From this plot the strain rate and spall strength was calculated. The average spall strength for the 250 μm thick monocrystalline tantalum sample was calculated to be ~9.0 GPa and the average strain rate was ~6 x 10^6 s^{-1}. Also shown is a velocity versus time profile for the single crystal 50 μm thick tantalum. Even thinner samples, ~30 μm thick, were laser shocked at similar intensities, but were unable to be recovered due to total obliterattion. The spall strength for the 50 μm thick single crystal Ta sample was ~11.6 GPa with a strain rate of ~ 2.5 x 10^7 s^{-1}. Sample thickness exhibits strong influence on the strain rate: the 50 μm thick sample achieved strain rates almost a 10-fold increase over that of the thicker samples of 250 μm.

Free surface velocity curves of single, poly and nanocrystalline Ta shows a clear grain size dependency relationship, as can be seen in Fig. 9. For a 250 μm thick polycrystalline tantalum sample the calculated average spall strength is ~8.2 GPa and average strain rate ~5.5 x 10^6 s^{-1}. The calculated average spall strength of a 250 μm thick nanocrystalline tantalum sample was ~7.0 GPa and the average strain rate was ~3.0 x 10^6 s^{-1}. Comparing these results (Fig. 10), single crystals have the highest spall strength, followed by polycrystals and nanocrystals, respectively. Spall strength was expected to be highest in single crystal and lowest in nanocrystal

because voids nucleate, grow and coalesce preferentially (leading to failure and spall) along grain boundaries. The SEM images attest to this logic. Thus, it is clear that the single crystals exhibit the highest spall strength since they have the fewest grain boundaries (none), and nanocrystals have the most, which leaves polycrystalline Ta spall strength to fall somewhere between the two.

4. Discussion

It has been shown in the previous section that tantalum exhibits ductile fracture behavior under dynamic loading. The spall strength increases as a function of the strain rate whereas it decreases with grain size, in agreement with experimental results in the literature [23,46]. The results of both molecular dynamics calculations and analytical modeling will be presented in Sections 4.1 and 4.2, respectively.

4.1 Molecular dynamics predictions

Our experimental results are in good agreement with the spall strength versus strain rate plot, Fig 11, which presents a broad range of both experimental and computational results. The open symbols represent the results of MD computations, which range from 10^{7} to 10^{12} s^{-1}; the closed circles come from a variety of sources, including flyer plate experiments at the lower strain rates, and the results of the current research. The monocrystalline specimens show a higher spall strength, especially at the lower strain rates. The three lines for monocrystalline, polycrystalline, and nanocrystalline spall strength converge at 10^{12} s^{-1}, which is close to the Debye frequency, corresponding to the frequency of atomic vibration. This was analyzed by Hahn et al.[13] and potentially considered the ultimate tensile strength. There is a group of experimental results at 10^{10} s^{-1}, which show values clearly higher than the current measurements. Hahn et al.[13] also explained the differences between mono and nanocrystalline tantalum tensile

failure through molecular dynamics. The presence of a grain boundary localizes the failure along the interface, although nucleation of voids also takes place in other regions. The growth is favored along the grain boundary, as can be seen in Figure 12a. Different grains are identified by characteristic colors; the atoms are colored qualitatively according to their local crystalline orientation. A void growing along a grain boundary is visible. Fig. 12b shows the process of void coalescence in a monocrystal. Figs. 12c,d show dislocations (green lines) and the surface of voids (dark red) identified by DXA [53] and coordination algorithms respectively. The principal voids are also surrounded by smaller voids in both cases. Failure in the nanocrystalline sample is limited to the grain boundaries, where the single crystal exhibits intragranular failure. The calculated spall strengths for nano and single-crystal tantalum at a strain rate of 10^8 s^{-1} are 8.5 and 13 GPa respectively. Thus, there is a significant reduction of spall strength when introducing a high volume fraction of boundaries.

4.1 Analysis of Void Nucleation, Growth, and Coalescence

It is clear from the observations that nucleation of voids takes place both in the grain interiors and boundaries, with specific and distinct nucleation/growth rates. The kinetics of their growth is also influenced by the presence of grain boundaries. Both effects are evident in Fig. 6c. The nucleation occurs in both grain interiors and boundaries; however, the coalescence of voids occurs preferentially along grain boundaries, leading to an intergranular fracture. These two effects are described graphically in schematic fashion in Figure 13, which shows sequences for void nucleation and growth in monocrystalline (Fig. 13a1-a4) and polycrystalline (Fig. 13b1-b4), tantalum subjected to dynamic tensile loading. In monocrystalline materials the voids nucleate randomly in the grain interior and the growth requires the plastic deformation of its surroundings. The voids grow via the emission of dislocations from the void/matrix interface.

The shadowed area in Fig. 13a1 illustrates the plastic zone in the vicinity of the void. Such voids are named intragranular. Voids continue to nucleate and grow in the material, resulting in a distribution of void sizes. Eventually, the voids coalesce and ductile failure takes place.

Void nucleation and growth at the grain boundaries is shown in Fig. 13b1-b4. The voids develop a non-spherical, oblate spheroid shape with the major axes aligned with the boundary plane. The plastic zone, for a specific diameter, tends to be smaller than for the intragranular voids. The energy required for intergranular void growth is thus smaller than that of for intragranular growth. Thus, as will be shown quantitatively later, intergranular voids dominate failure in polycrystalline materials.

The growth of voids is the result of shear and prismatic loop emission by a mechanism proposed by Lubarda et al. [47] and verified by molecular dynamics simulations in fcc and bcc metals [48, 49,50]. The growth along grain boundaries proceeds by the same mechanism but the number of loops emitted is less because of differences in shape (oblate spheroid vs. sphere). Figure 14a shows, in schematic fashion, the emission of shear and prismatic loops leading to the growth of voids in the grain interior.

It has been postulated analytically [47,48] and demonstrated by molecular dynamics calculations [e.g.,[49,50,53]] that growth of spherical voids takes place by dislocation emission from the void surface. These shear loops eventually form prismatic loops by cross-slipping of the screw (lateral) component, as the (frontal) edge component advances. This is shown in Fig. 14. In fcc metals, where partial dislocations are emitted, this reaction does not take place. Figure 14(a) shows the sequence of dislocation emission from a growing void in a bcc metal, starting with shear loops propagating in eight [111] directions and continuing with the formation of prismatic loops.

It is possible to equate the total length of dislocations to the volume of a void, and this has indeed been done by Ruestes et al. [51,52] and Hahn et al.[13]. The growth of a spherical void requires a greater dislocation length than an oblate spheroid with the same radius R. The emission of dislocations from a growing intergranular void is qualitatively shown in Fig. 14b.

A quantitative evaluation of the kinetics of void nucleation and growth is presented next, starting with spheroidal intragranular voids and proceeding to intergranular voids. The Curran-Seaman-Shockey (CSS) theory [15,16, 17] will be applied and extended to the polycrystalline regime. The number of voids in ductile metals is obtained from the nucleation rate per unit volume, $\dot{N}$, which was proposed by SSC to exhibit an exponential dependence and can be represented by:

$$\dot{N} = \dot{N}_0 exp\left(\frac{\sigma_m - \sigma_{no}}{\sigma_c}\right) \quad (3)$$

where σ_m is the tensile stress in the material, σ_{no} is the threshold stress for void nucleation, $\dot{N}_0$ is a reference nucleation rate, and σ_c is a material constant. The nucleation of voids has been reported to occur preferentially at twin boundaries; these twins are generated by the compressive wave that precedes the tensile pulse [53].

Formatted: Not Highlight

In addition to void nucleation, void growth is another factor that determines the spall behavior of ductile metals. Assuming a spherical void with a radius of *R*, the growth rate is the time derivative of the *R*, namely $\dot{R}$. Seaman et al. [55], proposed that the growth rate of the void is proportional to its radius R and is linearly dependent of the stress, above a threshold σ_{go}.

$$\frac{\dot{R}}{R} = k = \left(\frac{\sigma_m - \sigma_{go}}{4\eta}\right) \quad (4)$$

where σ_{go} is related to the stress for dislocation emission from an existing nucleus, $\eta = \frac{\tau}{\dot{\gamma}}$ is the material viscosity. Integrating Eqn. 4:

$$\dot{R}_\iota(t) = \dot{} ke^{kt} \quad (5)$$

As the voids grow, new voids nucleate in the fraction of the volume occupied by solid matter. For simplicity, we assume that $\sigma_{no} = \sigma_{go}$. We define damage as the ratio between the volume of voids and the total volume:

$$D = \frac{V_v}{V_0} \quad (6)$$

We then apply an analysis similar to that of the Johnson-Mehl-Avrami-Kolmogorov (JMAK) equations [56–60]. There is a critical difference. Whereas the growth velocity is constant in the JMAK treatment, it increases exponentially with time (Eqn. 5). First, we consider an extended volume, assuming that the material is completely solid and there is unlimited material available for voids to nucleate over the time interval $0<\tau<t$. The volume fraction change per unit volume is:

$$\frac{V_\beta^e}{V} = \frac{4}{3}\pi \dot{N}_o e^{\frac{\sigma-\sigma_{no}}{\sigma_1}} k^3 \phi(t) \quad (7)$$

Where $\phi(t)$ is given by:

$$\phi(t) = \frac{1}{3k}\left[\frac{2}{9k^3} + e^{3kt}(t^3 - \frac{t^2}{k} + \frac{2t}{3k^2} - \frac{2}{9k^3})\right] \quad (8)$$

We now consider the entire volume of material that becomes voids, by subtracting the void fraction of voids:

$$dV_v = dV_v^e \left(1 - \frac{V_v}{V_0}\right) \quad (9)$$

Integration and substitution into Eqn. 9 yields:

$$D = \frac{V_\beta}{V} = 1 - e^{\left[-\frac{4}{3}\pi \dot{N}_o e^{\frac{\sigma-\sigma_{no}}{\sigma_1}} k^3 \phi(t)\right]} \quad (10)$$

The detailed derivation is given in the Supplementary Information section.

Parameters can be obtained from the experiments and from values used by Seaman et al. [55] to develop an analytical prediction of damage as a function of time. Some of these are discussed below. The spacing between both intergranular and intragranular voids can be inferred from the dimple size shown in Fig. 6. Each dimple corresponds to one-half of a void, the other being in the matching surface. For the polycrystalline (intergranular voids) and monocrystalline (intragranular voids) spall surfaces, the spacing is ~1 μm. This provides N = 1μm^{-3}. The time was taken as 10 ns. The initial nucleation rate was taken as $\dot{N}_0$ =10^{-10}m^{-3}s^{-1}. The spall strength in gas-gun experiments, in which the pulse time is 100 times larger (1 μs vs. 10 ns) than laser experiments is equal to 4-6 GPa. This is used as a first estimate of $\sigma_{n0} = \sigma_{go}$ = 4 GPa. The normalizing parameter σ_c has to be evaluated from previous experiments by Seaman et al. [55]. This parameter has values of 0.2 GPa for copper and 0.04 GPa for Al. The former (σ_c=0.2 GPa) is used for tantalum. The viscosity η was taken as 0.127 and is extracted from Hahn et al. [13].

Coalescence of voids occurs when the void volume reaches a sufficiently large fraction. Deformation concentrates primarily in the ligaments between the voids. These eventually undergo necking and complete separation. We assume that this occurs at D = 0.5. Figure 15a shows the application of Equation 10 to tantalum. The sigmoidal shape is characteristic of the JMAK equation is apparent and is shown in Figure 15a. Note that as the stress increases, the curve is translated to shorter times.

For intergranular voids, we use a similar approach as before, except we assume that the voids formed across grain boundaries are oblate spheroids (whereas before we assumed perfect spheres). As a result, we define damage in a slightly modified manner:

$$D = \frac{A_v}{A_0} \tag{11}$$

Where A_v is the total area of intergranular voids in a grain-boundary surface area A_0. Intergranular void growth proceeds with the major axes of the oblate spheroid aligned with the grain-boundary plane. This opening along grain boundaries is the result of the competition between flow stress and grain-boundary cohesive strength, which have different strain rate sensitivities.

It will be shown that the growth of a grain-boundary void requires less plastic deformation than that of a grain-interior void. The plastic deformation regions are schematically shown in Fig. 14b.

It is possible to use the concept of geometrically necessary dislocations advanced by Ashby [61–63] to predict their density around a growing void. Traiviratana et al. [64], Ruestes et al. [51,52] and Hahn et al.[13] obtained expressions relating the growth of a void to the dislocation length generated by assuming an effective volume per dislocation equal to b^2 per unit length:

Formatted: Not Highlight

$$dV = 4\pi R^2 dR \qquad \text{and} \qquad dR = \frac{b^2 dL}{4\pi R^2} \tag{12}$$

Where dL is the increase in the length of dislocation line.

Thus, for a radius R_f of a void:

$$L_f = \frac{4\pi}{b^2}\int_0^{R_f} R^2\, dR = \frac{4\pi}{3b^2}R_f^3 \tag{13}$$

If one considers the plastic zone equal to nR, one can calculate the density of these geometrically-necessary dislocations:

$$\rho_{sphere} = \frac{3L_f}{(n^3-1)4\pi R_f^3} \quad (14)$$

Substituting Eqn. 13 into 14, we have:

$$\rho_{sphere} = \frac{1}{3b^2(n^3-1)} \quad (15)$$

For Ta, Hahn et al. [13] used b^2=0.106 nm^2 for dislocations under tensile loads. If one assumes that n=3, a reasonable value for the work hardened zone, one obtains $\rho = 4x10^{17} m^{-2}$, a reasonable number for a severely hard-worked metal. This is on the same order of magnitude than the values obtained by MD and calculated by procedure above.

For an intergranular void, the volume is:

$$V = \frac{4}{3}\pi a R^2 \quad (16)$$

Where a is the minor semi-axis of the oblate spheroid and R is its major axis. The dislocation density can be similarly be expressed as:

$$\rho_{spheroid} = \frac{a}{R}\rho_{sphere} \quad (17)$$

It is clear that the growth of grain-boundary voids requires less plastic deformation, and therefore less work, than that of grain-interior voids. We will use a simple expression relating the growth rate of the two types of voids; it essentially considers the rate of growth tied to the plastic work rate.

$$\frac{dR_{Gb}}{dt} = \frac{R}{a}\frac{dR_i}{dt} \quad (18)$$

Thus,

$$\dot{R_{Gb}}(t) = \dot{k}' e^{kt} \quad (19)$$

Where k'=(R/a)k. Considering self-similarity and a constant aspect ratio $l=a/R<1$ for the oblate spheroid:

$$\frac{dA_v}{dt} = 2\pi Rl\frac{dR_i}{dt} \quad (20)$$

The procedure outlined in Eqns. 7-10 can be applied for the intergranular case. The initial nucleation rate. The initial nucleation rate was taken as $\dot{N}_0 = 10^{-4} m^2 s^{-1}$. We assume that R/a is 2, and account for the ratio of areas rather than volumes. A complete derivation can be found in the supplemental information. Figure 15b shows that intergranular void growth approaches failure (D=0.5) more quickly than intragranular growth (Figure 15a).

By assuming spallation occurs at D = 0.5, the spall strength can be found and related to the strain rate. The corresponding spall strengths as a function of the tensile pulse duration are shown in Figure 16. It is clear that, although the two mechanisms of intergranular and intragranular failure are operating, intergranular overtakes intragranular spalling and the polycrystalline tantalum fails by grain-boundary separation. A corollary of this is that the monocrystalline tantalum exhibits a higher spall strength.

The strain rate can obtained from the duration of the pulse by the application of the following expression from Reina et al. [79] and Hahn et al. [13] based on dimensional analysis:

$$\frac{d\varepsilon}{dt} = \frac{U_p}{tC_l} \quad (21)$$

where U_p is the particle velocity (dependent on pressure) and C_l is the longitudinal sound velocity (5,400 m/s for Ta). The equation of state parameters used for the calculation of U_p as a function of pressure are obtained from Marsh [80]: U_s=3.43+1.19 U_p . For the analysis performed, we report the strain rate sensitivity at 0.51 for the intergranular case and 0.50 for the

intragranular case. Although these values are larger than those from molecular dynamics (Fig. 11), the current analysis applies to highly localized void growth and the values are dependent on the parameters chosen.

5. Conclusions

Mono, poly and nanocrystalline tantalum spall by ductile failure. Voids nucleate, grow and coalesce around grain boundaries in poly and nanocrystalline Ta; single crystalline Ta also shows signs of extensive dimpling. At lower strain rates of 10^6 s^{-1} (250 μm thick samples), single crystalline tantalum had the highest spall strength while nanocrystalline tantalum had the lowest, which has been explained by a past theory developed by Meyers [63]. Figure 15 shows a rationale for the differences in spall strength between the different conditions. The ultimate tensile response of Ta is represented by the ascending curves, which take into consideration the grain size and strain rate sensitivity. The same sort of relationship has been observed in Cu[64] and V[65]. This rationale is based on a lower strain-rate dependence for grain boundary separation because the rate-controlling mechanism is not the thermally-activated or drag-limited motion of dislocations. Polycrystals and nanocrystals contain boundaries, which act as heterogeneous nucleation sites for microvoids that nucleate and grow preferentially along the grain boundaries and, in the case of the polycrystals, may be related to the preferential segregation of impurities at the grain boundaries. Indeed, the grain-boundary nucleation stress can be considerably lower than the bulk nucleation stress. The crossover between the curves marks the change in failure from bulk to intergranular. The volumetric analysis of the spall surface, performed nondestructively using X-ray micro-CT, supports the observations of the spall surface and confirms that the polycrystalline samples spall via intergranular void nucleation, growth and coalescence.

X-ray micro-CT has demonstrated unique potential for characterizing the complex failure structures resulting from spall, even in the heavily attenuating tantalum system. Decreasing sample thickness (from 250 to 50 μm) resulted in higher strain rates (by ~10 fold) and spall strengths (~30% higher) than their thicker counterparts. Thus, a clear dependence of spall strength on strain rate and sample thickness was observed.

Molecular dynamics calculations predict spall strengths for mono and nanocrystalline tantalum, albeit at much smaller durations, that are consistent with the experimental results: the nucleation of voids occurs both inside (intra) and at the grain boundaries (intergranular), but the differences in the nucleation rates and growth rates lead to intergranular void coalescence and failure in the nanocrystalline specimens, with an attended decrease in the spall strength. The variation of the spall strength with strain rate for the three cases of mono, poly, and nanocrystals converge at strain rates of 10^{12} s^{-1}; this is close to the Debye frequency, which is presumably the highest strain rate achievable.

The Curran-Seaman-Shockey theory for spalling in ductile materials is applied to the experimental conditions in the present work and extended for intergranular nucleation, growth, and coalescence of voids. This theory provides an analytical underpinning for the differences observed between mono and polycrystals and captures the principal features of the failure.

In conclusion, a combined experimental-computational-analytical approach provides important new insights into the process of spalling in bcc metals, with tantalum as a model material.

Acknowledgements

This research was funded by the UC Research Laboratories Grant 09-LR-06-118456-MEYM, the SSAP NNSA grant DE-NA0002930, and the National Laser Users Facility Grant PE-FG52-09NA-29043. Experiments were performed at JLF, LLNL and the OMEGA laser facility, University of Rochester, New York. J.C.E. Mertens and N. Chawla acknowledge support from the Security and Defense Systems Initiative at Arizona State University. S. Sabbaghianrad and T.G. Langdon were supported by the U.S. National Science Foundation under Grant No. DMR-1160966. SEM was conducted at the Nano3 User Facility at the University of California, San Diego (UCSD). Target assembly was managed by UCSD in collaboration with The Schafer Corporation, General Atomics, and LLNL. A sincere thank you to Laura Chen, Zach Sternberger, and Yekaterina Opachich for overall assistance.

References

[1] R.J. Kurtz, M.L. Hamilton, H. Li, Grain boundary chemistry and heat treatment effects on the ductile-to-brittle transition behavior of vanadium alloys, J. Nucl. Mater. 258–263, Part 2 (1998) 1375–1379. doi:10.1016/S0022-3115(98)00161-5.

[2] S.J. Zinkle, H. Matsui, D.L. Smith, A.F. Rowcliffe, E. van Osch, K. Abe, V.A. Kazakov, Research and development on vanadium alloys for fusion applications, J. Nucl. Mater. 258–263, Part 1 (1998) 205–214. doi:10.1016/S0022-3115(98)00269-4.

[3] R.J. Kurtz, K. Abe, V.M. Chernov, V.A. Kazakov, G.E. Lucas, H. Matsui, T. Muroga, G.R. Odette, D.L. Smith, S.J. Zinkle, Critical issues and current status of vanadium alloys for fusion energy applications, J. Nucl. Mater. 283–287, Part 1 (2000) 70–78. doi:10.1016/S0022-3115(00)00351-2.

[4] T.P. Remington, B.A. Remington, E.N. Hahn, M.A. Meyers, Deformation and failure in extreme regimes by high-energy pulsed lasers: A review, Mater. Sci. Eng. A. 688 (2017) 429–458. doi:10.1016/j.msea.2017.01.114.

[5] M.A. Meyers, C. Taylor Aimone, Dynamic fracture (spalling) of metals, Prog. Mater. Sci. 28 (1983) 1–96. doi:10.1016/0079-6425(83)90003-8.

[6] Antoun, Spall Fracture, Springer New York, 2003. http://link.springer.com/chapter/10.1007/0-387-21516-6_1 (accessed July 27, 2014).

[7] W.J. Bruchey, Suppression of Material Failure Modes in Titanium Armors, 2003.

[8] S. Eliezer, I. Gilath, T. Bar‐Noy, Laser‐induced spall in metals: Experiment and simulation, J. Appl. Phys. 67 (1990) 715–724. doi:10.1063/1.345777.

[9] S. Eliezer, Y. Gazit, I. Gilath, Shock wave decay and spall strength in laser‐matter interaction, J. Appl. Phys. 68 (1990) 356–358. doi:10.1063/1.347142.

[10] T. de Rességuier, M. Hallouin, Stress relaxation and precursor decay in laser shock-loaded iron, J. Appl. Phys. 84 (1998) 1932–1938. doi:10.1063/1.368322.
[11] B.A. Remington, G. Bazan, J. Belak, E. Bringa, J.D. Colvin, M.J. Edwards, S.G. Glendinning, D.H. Kalantar, M. Kumar, B.F. Lasinski, K.T. Lorenz, J.M. McNaney, S.M. Pollaine, D. Rowley, J.S. Stölken, S.V. Weber, W.G. Wolfer, M. Caturla, D.S. Ivanov, L.V. Zhigilei, B. Kad, M.A. Meyers, M. Schneider, D.D. Meyerhofer, B. Yaakobi, J.S. Wark, Materials science under extreme conditions of pressure and strain rate, Metall. Mater. Trans. A. 35 (2004) 2587–2607. doi:10.1007/s11661-004-0205-6.
[12] M.S. Schneider, B. Kad, D.H. Kalantar, B.A. Remington, E. Kenik, H. Jarmakani, M.A. Meyers, Laser shock compression of copper and copper–aluminum alloys, Int. J. Impact Eng. 32 (2005) 473–507. doi:10.1016/j.ijimpeng.2005.05.010.
[13] E.N. Hahn, T.C. Germann, R. Ravelo, J.E. Hammerberg, M.A. Meyers, On the ultimate tensile strength of tantalum, Acta Mater. 126 (2017) 313–328. doi:10.1016/j.actamat.2016.12.033.
[14] E.N. Hahn, T.C. Germann, R.J. Ravelo, J.E. Hammerberg, M.A. Meyers, Non-equilibrium molecular dynamics simulations of spall in single crystal tantalum, AIP Conf. Proc. 1793 (2017) 070006. doi:10.1063/1.4971594.
[15] D. R. Curran, L. Seaman, and D. A. Shockey, Linking Dynamic Fracture to Microstructural Processes, in "Shock Waves and High-Strain-Rate Phenomena in Metals," eds. M. A. Meyers and L. E. Murr, Plenum Press, 1981,pp. 129-167.
[16] D.R. Curran, L. Seaman, D.A. Shockey, Dynamic failure of solids, Phys. Rep. 147 (1987) 253–388. doi:10.1016/0370-1573(87)90049-4.
[17] D.R. Curran, L. Seaman, Simplified Models of Fracture and Fragmentation, in: High-Press. Shock Compression Solids II, Springer, New York, NY, 1996: pp. 340–365. doi:10.1007/978-1-4612-2320-7_13.
[18] F.R. Tuler, B.M. Butcher, A criterion for the time dependence of dynamic fracture, Int. J. Fract. Mech. 4 (1968) 431–437. doi:10.1007/BF00186808.
[19] D.A. Shockey, D.C. Erlich, J.F. Kalthoff, H. Homma, Short-pulse fracture mechanics, Eng. Fract. Mech. 23 (1986) 311–319. doi:10.1016/0013-7944(86)90195-5.
[20] G. Kanel, V. Fortov, Mechanical properties of condensed media under high-intensity impact loading, Uspekhii Mekhaniki-Adv. Mech. 10 (1987) 3–82.
[21] D.E. Grady, The spall strength of condensed matter, J. Mech. Phys. Solids. 36 (1988) 353–384. doi:10.1016/0022-5096(88)90015-4.
[22] D.E. Grady, M.E. Kipp, Dynamic Fracture and Fragmentation, in: J.R. Asay, M. Shahinpoor (Eds.), High-Press. Shock Compression Solids, Springer New York, 1993: pp. 265–322. doi:10.1007/978-1-4612-0911-9_8.
[23] S.V. Razorenov, G.I. Kanel', G.V. Garkushin, O.N. Ignatova, Resistance to dynamic deformation and fracture of tantalum with different grain and defect structures, Phys. Solid State. 54 (2012) 790–797. doi:10.1134/S1063783412040233.
[24] J.P. Cuq-Lelandais, M. Boustie, L. Berthe, T. de Rességuier, P. Combis, J.P. Colombier, M. Nivard, A. Claverie, Spallation generated by femtosecond laser driven shocks in thin metallic targets, J. Phys. Appl. Phys. 42 (2009) 065402. doi:10.1088/0022-3727/42/6/065402.
[25] S.I. Ashitkov, P.S. Komarov, E.V. Struleva, M.B. Agranat, G.I. Kanel, K.V. Khishchenko, The behavior of tantalum under ultrashort loads induced by femtosecond laser, J. Phys. Conf. Ser. 653 (2015) 012001. doi:10.1088/1742-6596/653/1/012001.

[26] B. Albertazzi, N. Ozaki, V. Zhakhovsky, A. Faenov, H. Habara, M. Harmand, N. Hartley, D. Ilnitsky, N. Inogamov, Y. Inubushi, T. Ishikawa, T. Katayama, T. Koyama, M. Koenig, A. Krygier, T. Matsuoka, S. Matsuyama, E. McBride, K.P. Migdal, G. Morard, H. Ohashi, T. Okuchi, T. Pikuz, N. Purevjav, O. Sakata, Y. Sano, T. Sato, T. Sekine, Y. Seto, K. Takahashi, K. Tanaka, Y. Tange, T. Togashi, K. Tono, Y. Umeda, T. Vinci, M. Yabashi, T. Yabuuchi, K. Yamauchi, H. Yumoto, R. Kodama, Dynamic fracture of tantalum under extreme tensile stress, Sci. Adv. 3 (2017) e1602705. doi:10.1126/sciadv.1602705.
[27] C.H. Lu, B.A. Remington, B.R. Maddox, B. Kad, H.S. Park, M. Kawasaki, T.G. Langdon, M.A. Meyers, Laser compression of nanocrystalline tantalum, Acta Mater. 61 (2013) 7767–7780. doi:10.1016/j.actamat.2013.09.016.
[28] R.B. Figueiredo, P.H.R. Pereira, M.T.P. Aguilar, P.R. Cetlin, T.G. Langdon, Using finite element modeling to examine the temperature distribution in quasi-constrained high-pressure torsion, Acta Mater. 60 (2012) 3190–3198. doi:10.1016/j.actamat.2012.02.027.
[29] N. Maury, N.X. Zhang, Y. Huang, A.P. Zhilyaev, T.G. Langdon, A critical examination of pure tantalum processed by high-pressure torsion, Mater. Sci. Eng. A. 638 (2015) 174–182. doi:10.1016/j.msea.2015.04.053.
[30] J.C.E. Mertens, J.J. Williams, N. Chawla, Development of a lab-scale, high-resolution, tube-generated X-ray computed-tomography system for three-dimensional (3D) materials characterization, Mater. Charact. 92 (2014) 36–48. doi:10.1016/j.matchar.2014.03.002.
[31] J.C.E. Mertens, J.J. Williams, N. Chawla, Note: Design and construction of a multi-scale, high-resolution, tube-generated X-Ray computed-tomography system for three-dimensional (3D) imaging, Rev. Sci. Instrum. 85 (2014) 016103. doi:10.1063/1.4861924.
[32] J.T. Larsen, S.M. Lane, HYADES—A plasma hydrodynamics code for dense plasma studies, J. Quant. Spectrosc. Radiat. Transf. 51 (1994) 179–186. doi:10.1016/0022-4073(94)90078-7.
[33] L. Tollier, R. Fabbro, E. Bartnicki, Study of the laser-driven spallation process by the velocity interferometer system for any reflector interferometry technique. I. Laser-shock characterization, J. Appl. Phys. 83 (1998) 1224–1230. doi:10.1063/1.366819.
[34] E. Dekel, S. Eliezer, Z. Henis, E. Moshe, A. Ludmirsky, I.B. Goldberg, Spallation model for the high strain rates range, J. Appl. Phys. 84 (1998) 4851–4858. doi:10.1063/1.368727.
[35] G.I. Kanel, S.V. Razorenov, A. Bogatch, A.V. Utkin, V.E. Fortov, D.E. Grady, Spall fracture properties of aluminum and magnesium at high temperatures, J. Appl. Phys. 79 (1996) 8310–8317.
[36] G.I. Kanel, S.V. Razorenov, A.V. Utkin, V.E. Fortov, K. Baumung, H.U. Karow, D. Rusch, V. Licht, Spall strength of molybdenum single crystals, J. Appl. Phys. 74 (1993) 7162–7165. doi:10.1063/1.355032.
[37] G.T. Gray III, N.K. Bourne, V. Livescu, C.P. Trujillo, S. MacDonald, P. Withers, The influence of shock-loading path on the spallation response of Ta, J. Phys. Conf. Ser. 500 (2014) 112031. doi:10.1088/1742-6596/500/11/112031.
[38] S. Plimpton, Fast Parallel Algorithms for Short-Range Molecular Dynamics, J. Comput. Phys. 117 (1995) 1–19. doi:10.1006/jcph.1995.1039.
[39] R. Ravelo, T.C. Germann, O. Guerrero, Q. An, B.L. Holian, Shock-induced plasticity in tantalum single crystals: Interatomic potentials and large-scale molecular-dynamics simulations, Phys. Rev. B. 88 (2013) 134101. doi:10.1103/PhysRevB.88.134101.

[40] Y.B. Zel'dovich, Y.P. Raizer, Physics of Shock Waves and High-Temperature Hydrodynamic Phenomena, Vol. I (1966) and Vol. II (1967), Academic Press, New York. Reprinted in a single volume by Dover Publications, Mineola, New York, 2002.
[41] A. Bushman, Intense dynamic loading of condensed matter Taylor & Francis, London, 1993.
[42] J.C.E. Mertens, J.J. Williams, N. Chawla, A Study of Pb-Rich Dendrites in a Near-Eutectic 63Sn-37Pb Solder Microstructure via Laboratory-Scale Micro X-ray Computed Tomography (μXCT), J. Electron. Mater. 43 (2014) 4442–4456. doi:10.1007/s11664-014-3382-0.
[43] G.T. Herman, Correction for beam hardening in computed tomography, Phys. Med. Biol. 24 (1979) 81. doi:10.1088/0031-9155/24/1/008.
[44] D. Prell, Y. Kyriakou, W.A. Kalender, Comparison of ring artifact correction methods for flat-detector CT, Phys. Med. Biol. 54 (2009) 3881. doi:10.1088/0031-9155/54/12/018.
[45] E. M. Bringa, S. Traiviratana, M. A. Meyers, Void Initiation in FCC Metals: Effect of Loading Orientation and Nanocrystalline Effects, Acta Mat, Vol. 58, pp. 4458-4477, 2010.
[46] S.A. Abrosimov, A.P. Bazhulin, V.V. Voronov, A.A. Geras'kin, I.K. Krasyuk, P.P. Pashinin, A.Y. Semenov, I.A. Stuchebryukhov, K.V. Khishchenko, V.E. Fortov, Specific features of the behaviour of targets under negative pressures created by a picosecond laser pulse, Quantum Electron. 43 (2013) 246–251. doi:10.1070/QE2013v043n03ABEH015106.
[47] V.A. Lubarda, M.S. Schneider, D.H. Kalantar, B.A. Remington, M.A. Meyers, Void growth by dislocation emission, Acta Mater. 52 (2004) 1397–1408. doi:10.1016/j.actamat.2003.11.022.
[48] J. Marian, J. Knap, M. A. Ortiz, Acta Mater 53(2005) 2893.
[49] Y. Tang, E.M. Bringa, M.A. Meyers, Ductile tensile failure in metals through initiation and growth of nanosized voids, Acta Mater. 60 (2012) 4856–4865. doi:10.1016/j.actamat.2012.05.030
[50] Y. Tang, E.M. Bringa, B.A. Remington, M.A. Meyers, Growth and collapse of nanovoids in tantalum monocrystals, Acta Mater. 59 (2011) 1354–1372. doi:10.1016/j.actamat.2010.11.001.
[51] C.J. Ruestes, E.M. Bringa, A. Stukowski, J.F. Rodríguez Nieva, Y. Tang, M.A. Meyers, Plastic deformation of a porous bcc metal containing nanometer sized voids, Comput. Mater. Sci. 88 (2014) 92–102. doi:10.1016/j.commatsci.2014.02.047.
[52] C.J. Ruestes, E.M. Bringa, A. Stukowski, J.F. Rodríguez Nieva, G. Bertolino, Y. Tang, M.A. Meyers, Atomistic simulation of the mechanical response of a nanoporous body-centered cubic metal, Scr. Mater. 68 (2013) 817–820. doi:10.1016/j.scriptamat.2013.01.035.
[53] G. T. Gray III, "High-strain-rate deformation: mechanical behavior and deformation substructures induced," Annu. Rev. Mater. Res. 42, 285–303 (2012)
[54] H.-J. Chang, J. Segurado, J. LLorca, Three-dimensional dislocation dynamics analysis of size effects on void growth, Scr. Mater. 95 (2015) 11–14. doi:10.1016/j.scriptamat.2014.09.018.
[55] L. Seaman, D.R. Curran, D.A. Shockey, Computational models for ductile and brittle fracture, J. Appl. Phys. 47 (1976) 4814–4826. doi:10.1063/1.322523.
[56] W. Johnson, R. Mehl, Reaction kinetics in processes of nucleation and growth, Trans. Metall. Soc. AIME. 135 (1939) 416–442.

[57] A.N. Kolmogorov, On the statistical theory of the crystallization of metals, Bull Acad Sci USSR Math Ser. 1 (1937) 355–359.
[58] M. Avrami, Kinetics of Phase Change. III : Granulation, Phase Change and Microstructure, J. Chem. Phys. 9 (1941) 177–184. doi:10.1063/1.1750872.
[59] M. Avrami, Kinetics of Phase Change. II Transformation‐Time Relations for Random Distribution of Nuclei, J. Chem. Phys. 8 (1940) 212–224. doi:10.1063/1.1750631.
[60] M. Avrami, Kinetics of Phase Change. I General Theory, J. Chem. Phys. 7 (1939) 1103–1112. doi:10.1063/1.1750380.
[61] M.F. Ashby, The deformation of plastically non-homogeneous materials, Philos. Mag. 21 (1970) 399–424. doi:10.1080/14786437008238426.
[62] M.F. Ashby, L. Johnson, On the generation of dislocations at misfitting particles in a ductile matrix, Philos. Mag. J. Theor. Exp. Appl. Phys. 20 (1969) 1009–1022. doi:10.1080/14786436908228069.
[63] M.F. Ashby, S.H. Gelles, L.E. Tanner, The stress at which dislocations are generated at a particle-matrix interface, Philos. Mag. J. Theor. Exp. Appl. Phys. 19 (1969) 757–771. doi:10.1080/14786436908216332.
[64] S. Traiviratana, E. M. Bringa, D. J. Benson, and M. A. Meyers, Void growth in metals: Atomistic calculations, Acta mat., Vol. 56, pp. 3874-3886, 2008.
[65] M.A. Meyers, R.W. Armstrong, H.O. Kirchner, Mechanics and materials: fundamentals and linkages, Wiley-VCH, 1999.
[66] R.W. Minich, J.U. Cazamias, M. Kumar, A.J. Schwartz, Effect of microstructural length scales on spall behavior of copper, Metall. Mater. Trans. A. 35 (2004) 2663–2673. doi:10.1007/s11661-004-0212-7.
[67] H. Jarmakani, B. Maddox, C.T. Wei, D. Kalantar, M.A. Meyers, Laser shock-induced spalling and fragmentation in vanadium, Acta Mater. 58 (2010) 4604–4628. doi:10.1016/j.actamat.2010.04.027.
[68] S. Zhao, B. Kad, E.N. Hahn, B.A. Remington, C.E. Wehrenberg, C.M. Huntington, H.-S. Park, E.M. Bringa, K.L. More, M.A. Meyers, Pressure and shear-induced amorphization of silicon, Extreme Mech. Lett. 5 (2015) 74–80. doi:10.1016/j.eml.2015.10.001.
[69] J.-P. Cuq‐Lelandais, M. Boustie, L. Soulard, L. Berthe, A. Sollier, J. Bontaz‐Carion, P. Combis, T. de Rességuier, E. Lescoute, Comparison Between Experiments And Molecular Dynamic Simulations Of Spallation Induced By Ultra‐Short Laser Shock On Micrometric Tantalum Targets, in: AIP Conf. Proc., AIP Publishing, 2009: pp. 829–832. doi:10.1063/1.3295270.
[70] L. Soulard, J. Bontaz-Carion, J.P. Cuq-Lelandais, Experimental and numerical study of the tantalum single crystal spallation, Eur. Phys. J. B. 85 (2012) 1–15. doi:10.1140/epjb/e2012-30269-9.
[71] T.P. Remington, Extreme Response in Tension and Compression of Tantalum, Ph.D. Thesis, University of California San Diego, 2015. http://www.escholarship.org/uc/item/42d8330s.
[72] Q. An, R. Ravelo, T.C. Germann, W.Z. Han, S.-N.N. Luo, D.L. Tonks, I.I.I. W. A. Goddard, Shock compression and spallation of single crystal tantalum, AIP Conf. Proc. 1426 (2012) 1259–1262. doi:10.1063/1.3686509.
[73] A.K. Zurek, W.R. Thissell, J.N. Johnson, D.L. Tonks, R. Hixson, Micromechanics of spall and damage in tantalum, J. Mater. Process. Technol. 60 (1996) 261–267. doi:10.1016/0924-0136(96)02340-0.

Formatted: Not Highlight

[74] G. Roy, Vers une modélisation approfondie de l'endommagement ductile dynamique: investigation expérimentale d'une nuance de tantale et développements théoriques, Ph.D. Thesis, Poitiers, 2003.
[75] J.M. Rivas, A.K. Zurek, W.R. Thissell, D.L. Tonks, R.S. Hixson, Quantitative description of damage evolution in ductile fracture of tantalum, Metall. Mater. Trans. A. 31 (2000) 845–851. doi:10.1007/s11661-000-1004-3.
[76] B. Glam, M. Werdiger, Y. Horovitz, E. Moshe, S.L. Pistinner, Dynamic strength of tantalum under impact, J. Phys. Conf. Ser. 500 (2014) 112029. doi:10.1088/1742-6596/500/11/112029.
[77] J.C.F. Millett, G. Whiteman, N.T. Park, S. Case, N.K. Bourne, The role of cold work on the shock response of tantalum, J. Appl. Phys. 113 (2013) 233502. doi:10.1063/1.4810896.
[78] A. Stukowski, K. Albe, Extracting dislocations and non-dislocation crystal defects from atomistic simulation data, Model. Simul. Mater. Sci. Eng. 18 (2010) 085001. doi:10.1088/0965-0393/18/8/085001.
[79] S. Christy, H. Pak, M. Meyers, Metallurgical applications of shock wave and high-strain-rate phenomena, N. Y. Basel. (1986).
[80] C. Reina, J. Marian, and M. Ortiz, Nanovoid nucleation by vacancy aggregation and vacancy-cluster coarsening in high-purity metallic single crystals, Physical Review B 84, (2011) 104117.
[81] S. P. Marsh, ed. , LASL Shock Hugoniot Data,U. of California Press, 1981, p. 132.

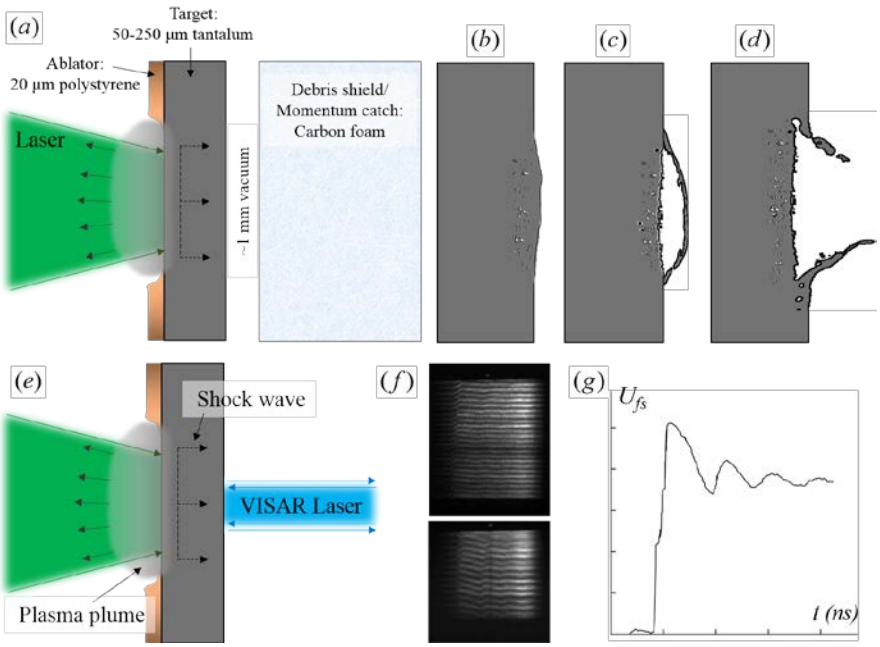

Figure 1. Experimental setup schematic. Tantalum discs of thickness ranging from 50 to 250 μm are covered by a 20 μm ablator/heat shield and subject to laser ablation in order to drive a planar shock wave through the system. (a-d) Recovery experiments used a carbon aerogel foam to catch debris, decelerate and catch the tantalum for characterization. Depending on the laser energy, three states are expected (b) initial stages of incipient spall to identify void nucleation; (c) intermediate incipient spall where a clear spall bubble can be evaluated for void nucleation and growth; (d) complete spall failure. (e-f) VISAR analysis of free surface velocity. (f) Fringes are captured by a streak camera where Fourier analysis can transform this data into the form presented in (g). Experiments were conducted at the Janus laser facility, LLNL.

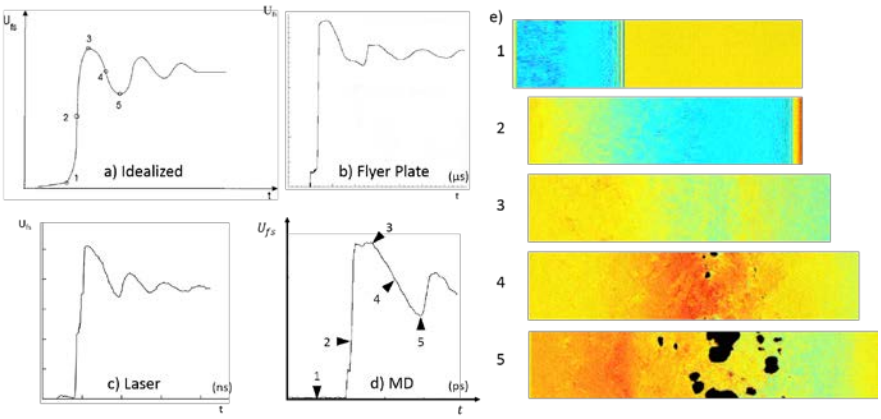

Figure 2. Free (rear) surface velocity as a function of time for tantalum. (a) Idealized, (b) flyer plate impact, (c) laser driven, and (d) molecular dynamics simulation. Each trace shows qualitative similarities and (e) highlights processes occurring inside the material at five characteristic points. Notable, void nucleation (4) begins approximately half way between the peak (3) and the pullback trough (5). The simulation is colored semi-qualitatively to the longitudinal shock stress state: blue is compression, red is tension, and yellow represents intermediate stress states.

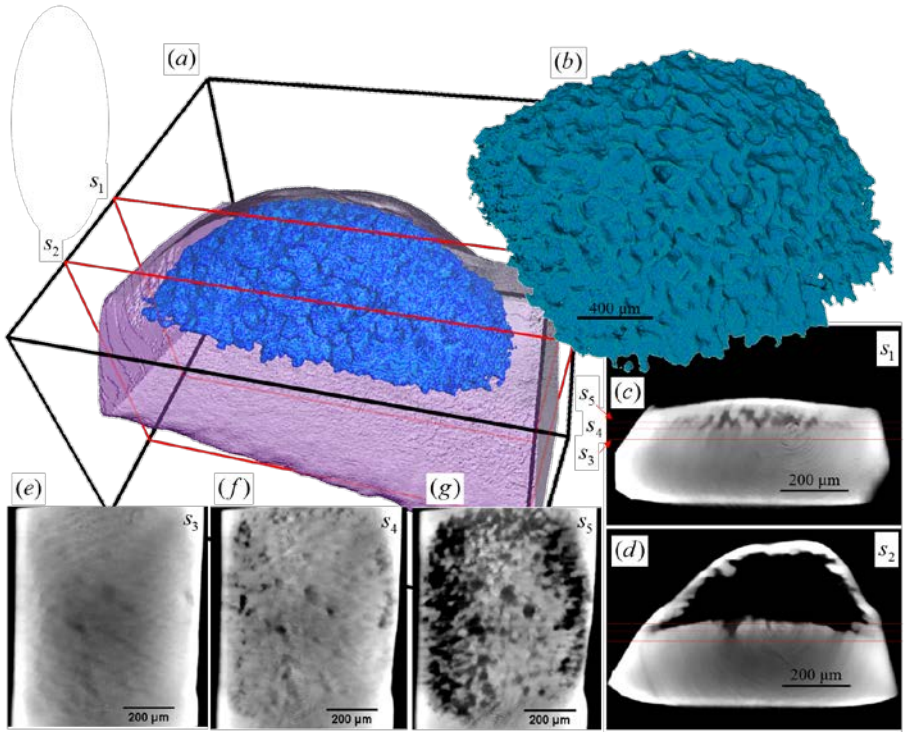

Figure 3. Segmented 3D volume derived from µ-CT imaging of the polycrystalline tantalum system subjected to spall conditions where the transparent purple is the tantalum and the solid blue material is the contained void. The surface of the spall bubble is shown in (b). (c,d) Cross sections identified in (a) showing (c) a view through the lateral edge of the spall bubble and (d) the center of the spall bubble. In (c,d) there is clear evidence of failure at grain boundaries by the presence of intact grains at the top and bottom of the bubble. Three "depth" progression views (e-g) correspond to the red lines of (c,d), laying parallel to the spall plane. Starting (e) near the edge of the spall bubble just within the tantalum, and going (f) 30 µm toward the bubble from part 'e', and (g) 50 µm toward the bubble from part 'e'.

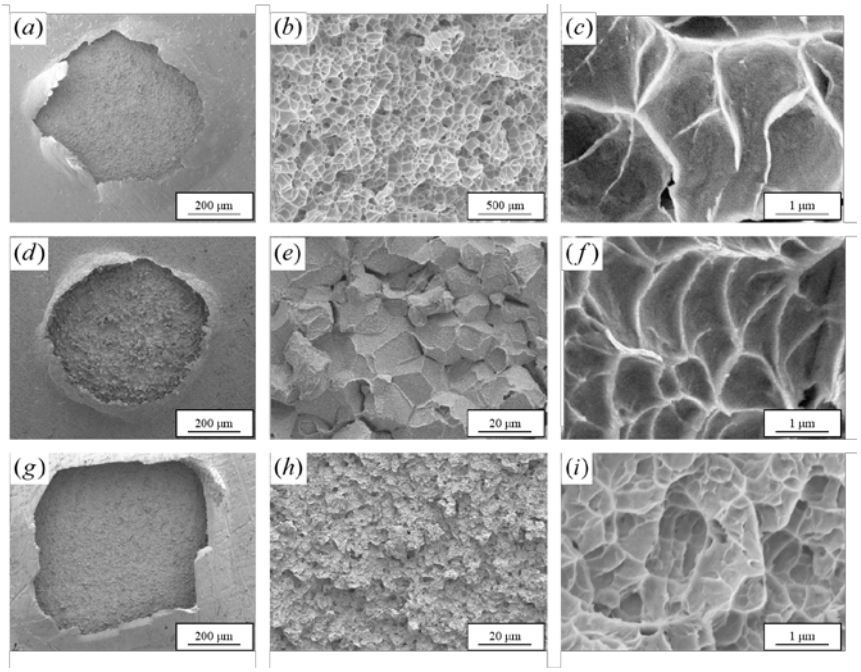

Figure 4. SEM images of single (a-c), poly (d-f) and nanocrystalline (g-i) tantalum showing complete ductile spallation. Ductile failure is evidenced by the dimpling observed in (c, f, and i).

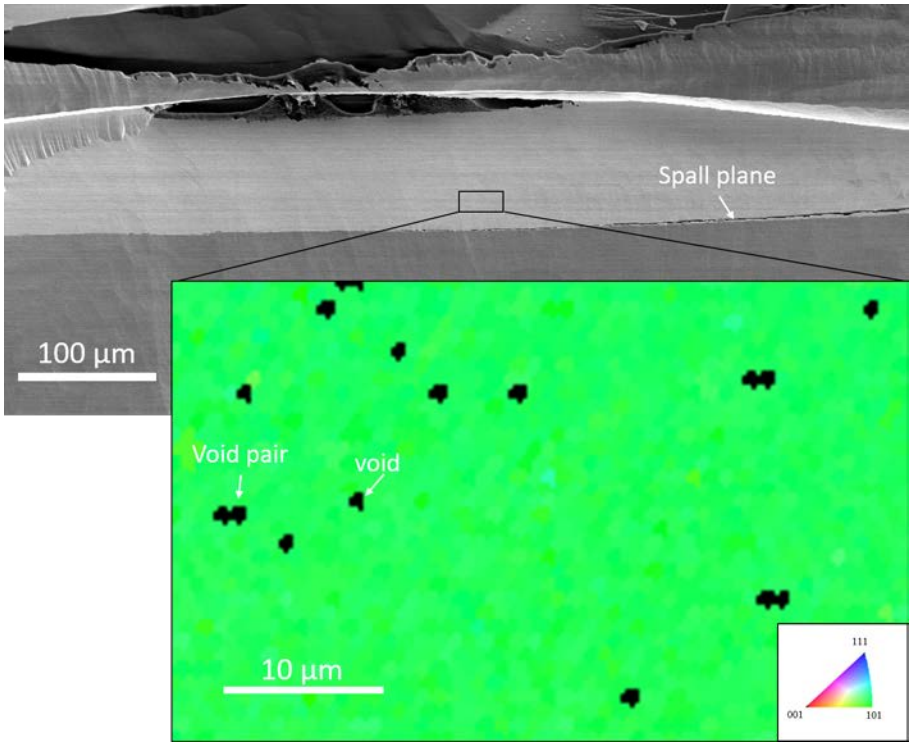

Figure 5. Microstructural analysis of monocrystalline tantalum spallation. The secondary electron SEM image on top shows the spall plane in the bottom of sample. The EBSD mapping (IPF) below shows randomly distributed voids in the vicinity of the spall plane; their spacing is approximately 10 µm.

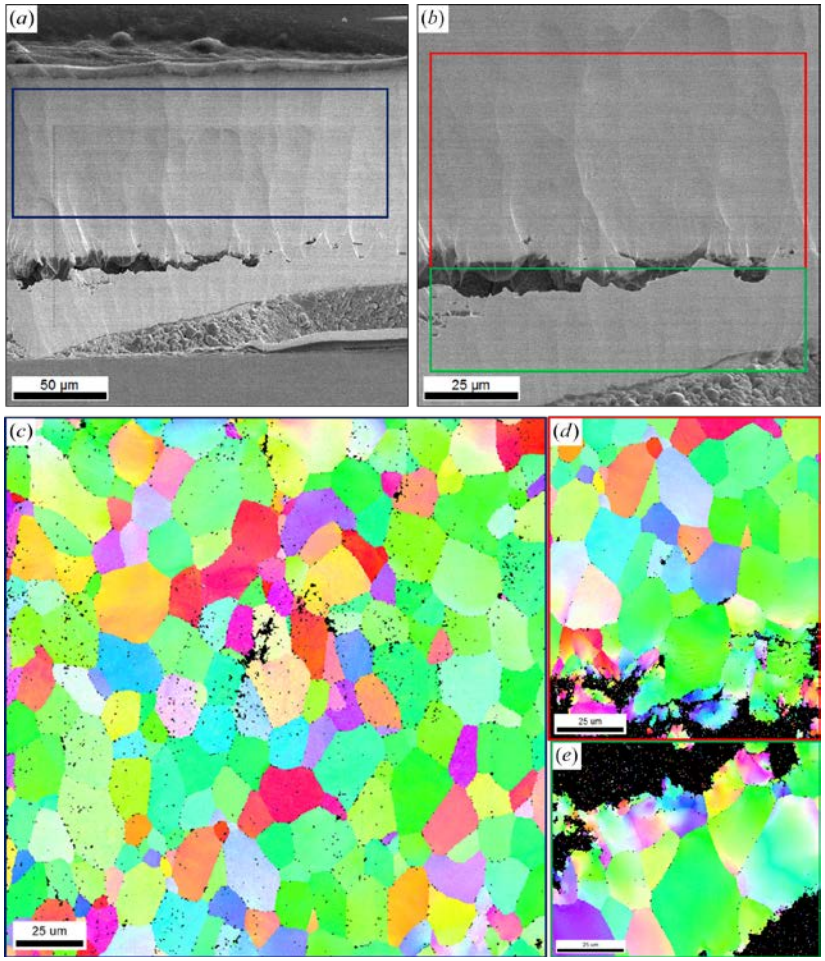

Figure 6. Microstructural analysis of polycrystalline tantalum spallation. The colored regions in figures (a,b) correspond to (c,d,e). (c) Away from the spall bubble, incipient spall can be seen as voids scattered throughout the specimen. The EBSD scans show the voids at the grain boundaries and with a few voids within the grains themselves. Voids within the grains can be attributed to defects present before laser shock inducing spalling. (d,e) The area directly beneath the spall bubble shows smaller grain sizes at the edge of the spall bubble. This can be attributed to the following: the voids growing relatively large from the imperfection sites within the grains at some point grew into the coalescing large voids growing at the grain boundaries. Once a large enough perforation was formed, the material pulled off (spalled off) leaving behind remnants of the grains, which are thus smaller in size than the average grain size of ~20 μm.

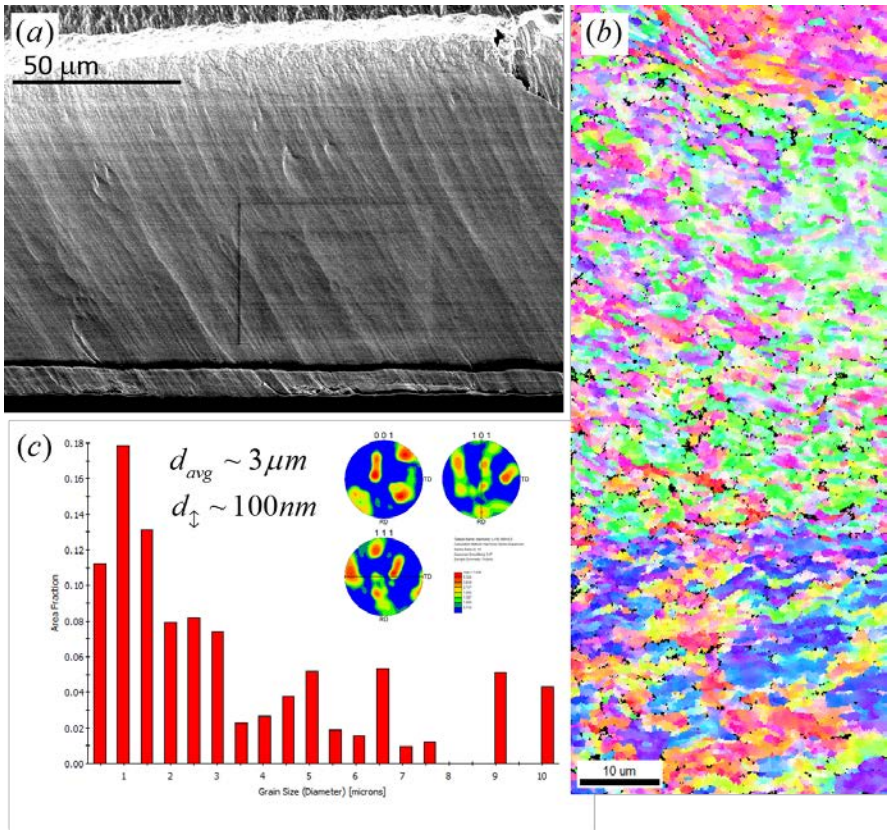

Figure 7. Microstructural analysis of nanocrystalline tantalum spallation. (a) The bottom surface shows a separation of the material. This separation suggests the voids that nucleated and had enough time to grow and coalesce into a large void volume. (b) In the adjacent region, the majority of voids can be found at nanocrystalline grain boundaries. From the scan, void nucleation, coalescence, and void clusters are most abundant at the grain interfaces, yet no particular crystalline orientation seems prevalent. (c) Grain size distribution and inverse pole figure (IPF) scan inset. Though the average grain size is 3 μm, the average grain size in the shock direction is 100 nm. The IPF shows significant texture, but there is no pre-shock reference with which to compare texture evolution during the spall process.

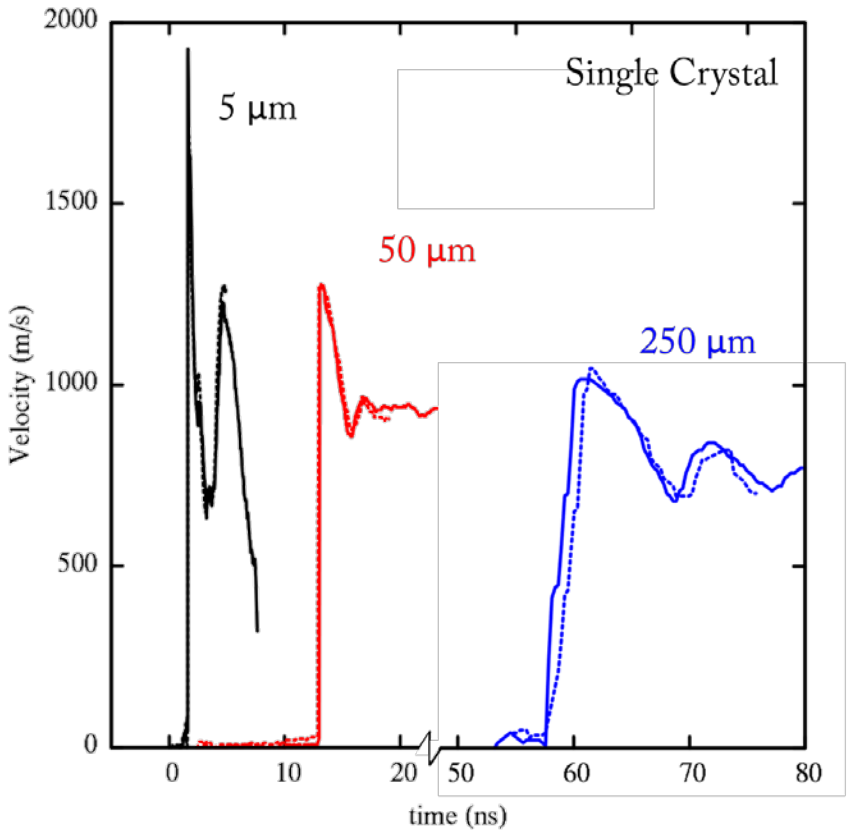

Figure 8. Free surface velocity traces for single crystals of varying thickness. 5 µm data from experiments conducted by C.E. Wehrenberg and details can be found in Zhao et al. [66].

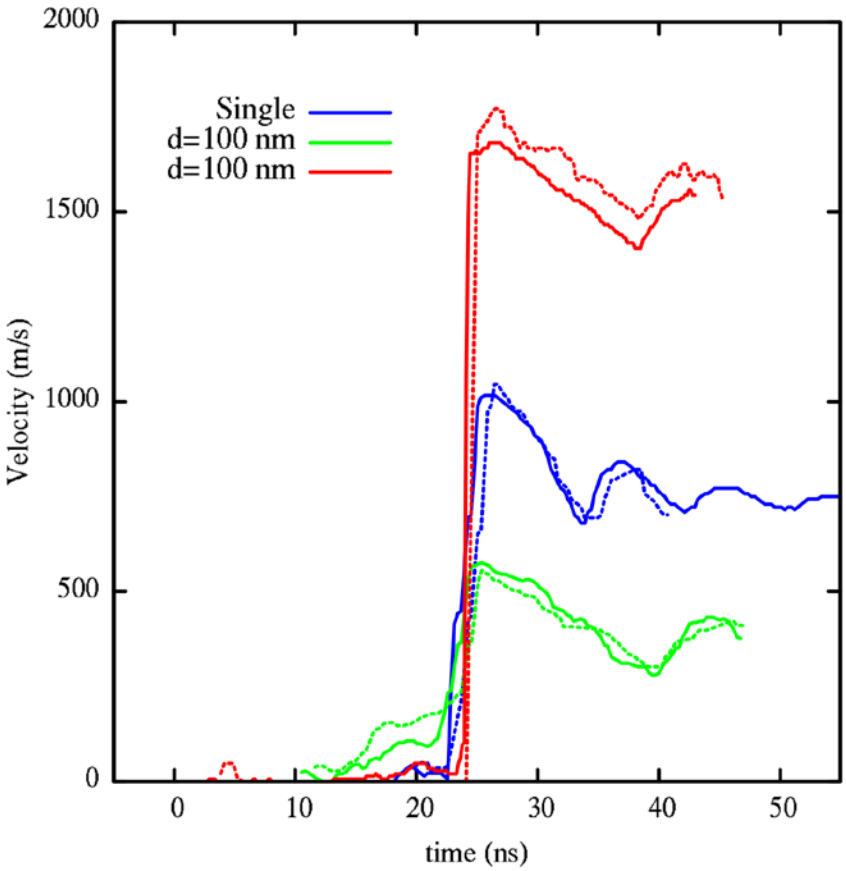

Figure 9. Representative VISAR traces for single and nanocrystalline tantalum. Although the current experiments were not able to match the peak shock pressure between single and nanocrystalline samples, the two nanocrystalline traces show similar pullback behavior and a decrease in pullback amplitude as compared to the single crystal. This indicates that monocrystal tantalum has a greater spall strength than nanocrystalline tantalum.

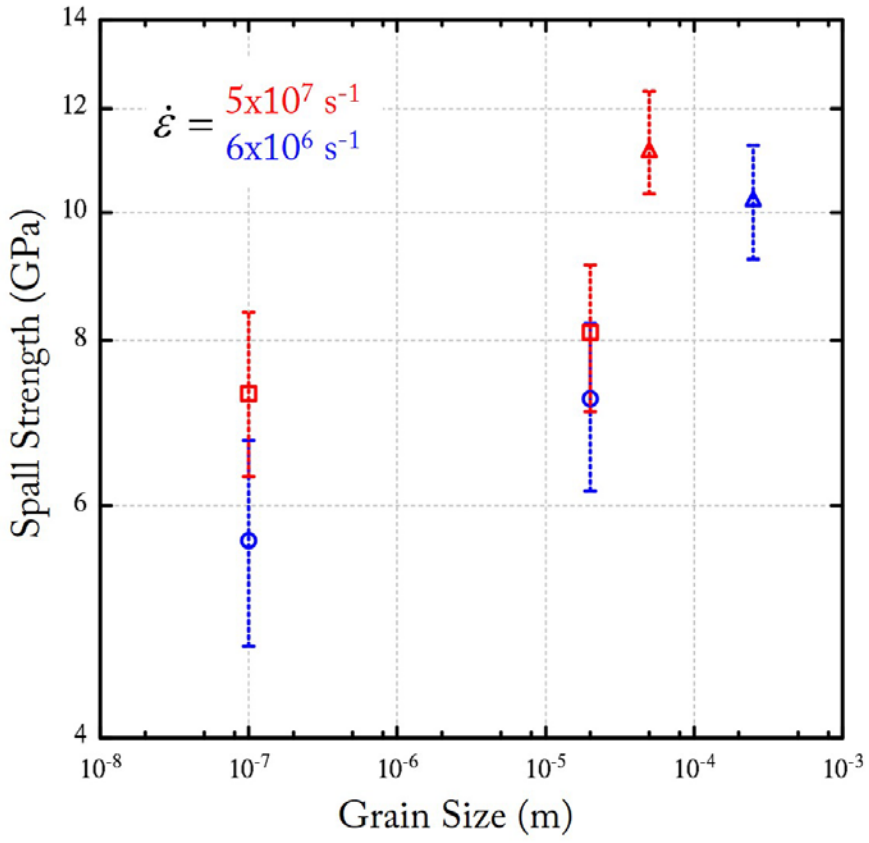

Figure 10. Experimental data shows there is a correlation between spall strength and grain size in tantalum. As grain size increases, spall strength increases in Ta.

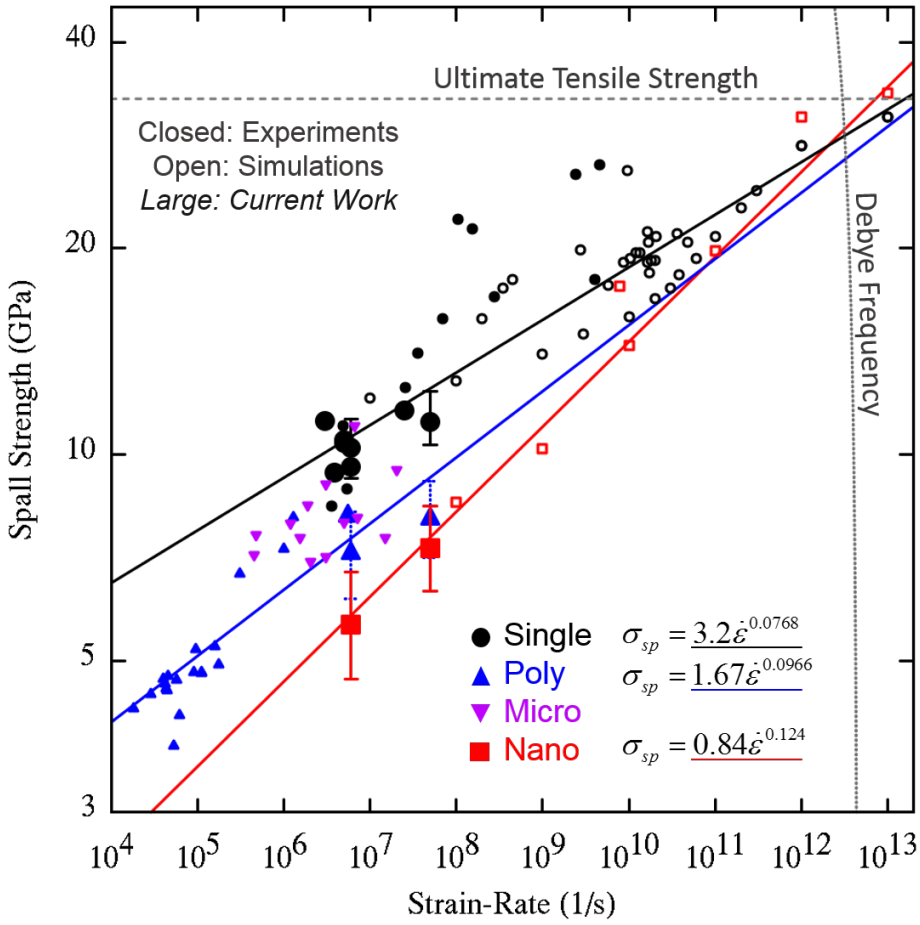

Figure 11. Spall strength as a function of strain rate plotted on a log-log scale. Power-law relationships are given for three "grain-sizes": single crystals, polcrystals (d > 5 um), and nanocrystals (d < 500 nm) (no fit is given for Microcrystals (500 nm > d > 5 um)). The ultimate tensile strength (UTS) of ~33 GPa is evaluated by Hahn et al. [13] using EOS and DFT data. The Debye frequency can be used as a predictor of what strain rate the material will reach the UTS and matches well with the power-law extrapolations. This graph illustrates the importance of the present nano-crystalline experiments in gaining insight into the grain-size dependent spall strength. Experimental data for large single and nanocrystalline samples (and thus lower strain rate) are absent from the literature. References as follows: Cuq-Lelandias et al.[24,67,68]; Abrosimov et al.[46]; Ashitkov et al.[25]; Zhao et al.[66] citing unpublished results from C. Wehrenberg; Razorenov et al.[23]; T. Remington's thesis[69]; Q. An et al.[70]; Gray et al.[37]; Zurek et al.[71]; G. Roy's thesis[72]; Rivas et al.[73]; Glam et al.[74]; and Millet et al.[75].

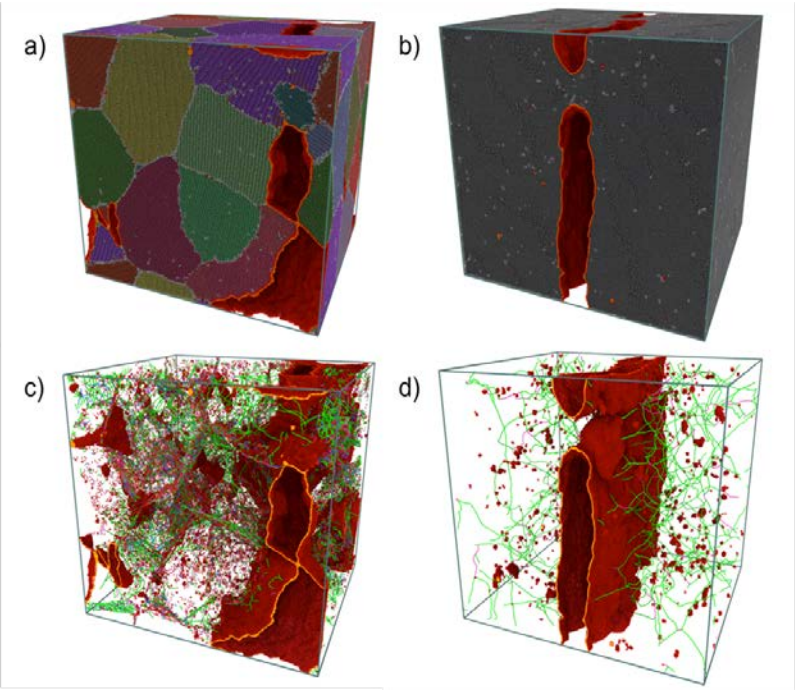

Figure 12. Molecular dynamics snapshots of spall failure in nano- and single-crystalline tantalum. The loading direction is from the left to the right and the nominal strain rate is 10^8 s^{-1}. a,c) 25 nm nano-crystalline tantalum. b,d) Single-crystalline tantalum. The top row shows atoms colored according to their local crystalline orientation. The bottom row shows dislocations and the surface of voids identified by DXA [76] and coordination algorithms respectively. In both images the surface of voids are denoted by a dark red color. Failure in the nano crystalline sample is limited to the grain boundaries, where the single crystal exhibits intragranular failure by necessity. The resulting spall strengths for nano and single-crystal tantalum at this strain rate are 8.5 and 13 GPa respectively - a 35% reduction of spall strength when introducing a high volume fraction of boundaries.

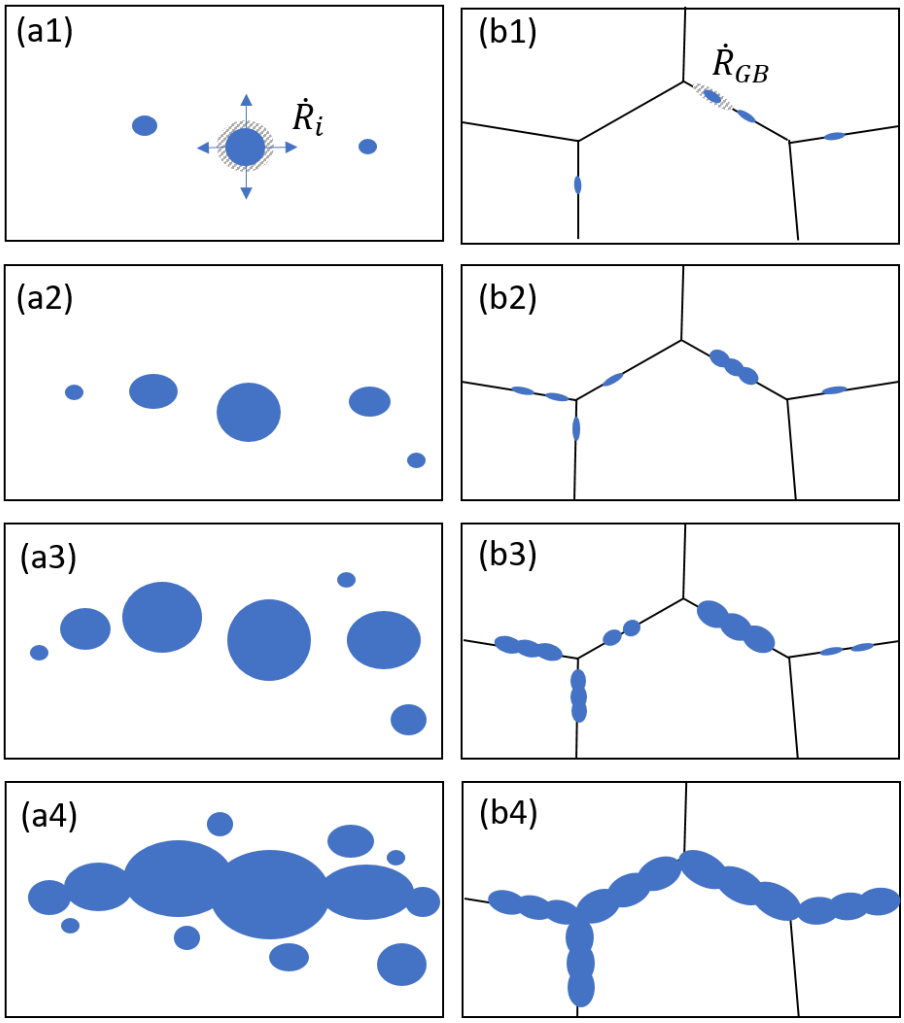

Figure 13 Schematic drawings of the void nucleation, growth, and coalescence in monocrystalline (a1-a4) and polycrystalline (b1-b4) samples. In monocrystalline samples, voids nucleate in the grain interiors and grow via the emission of dislocations from the void/matrix interface. The shadowed area in Fig. a1 illustrates the plastic zone in the vicinity of the void. Such voids named are called intragranular. Foer nucleation of voids at grain boundaries (Fig. 13 b1), they tend to develop a non-spherical, oblate spheroid shape with the major axes aligned with the boundary plane. The plastic zone, for a specific diameter, tends to be smaller. The energy required for intergranular void growth is thus smaller than that of for intragranular growth. Therefore, intergranular voids dominate failure in polycrystalline materials.

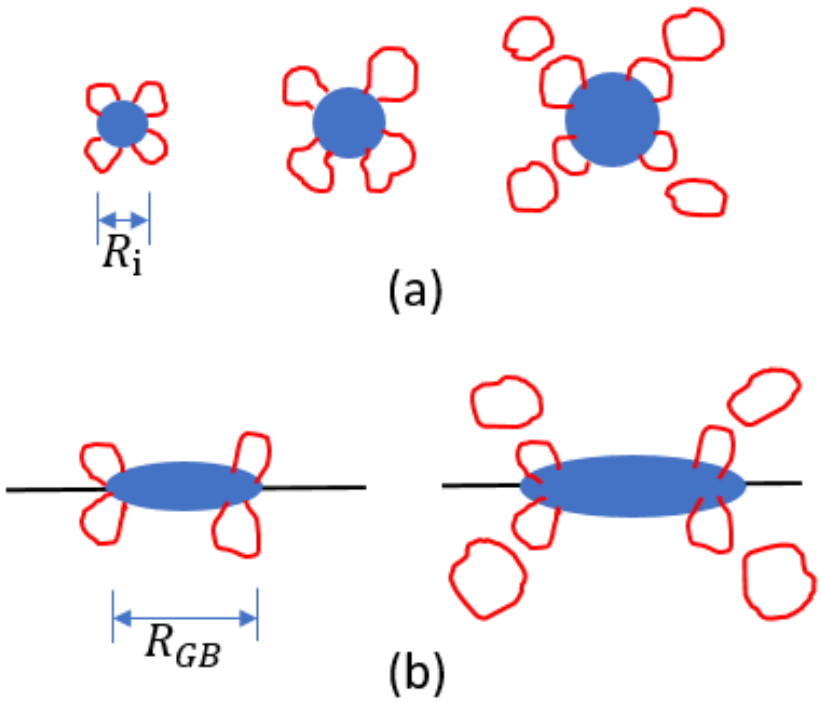

Figure 14. Schematic drawing of the void growth in grain interior and grain boundary. The emission of dislocations from these voids transports matter away from void and creates a work hardened layer. (a) In the grain interior (and monocrystals), shear loops are emitted from the void surface and propagate along eight {111} directions; they expand and pinch out prismatic loops through cross-slip of the screw components. (b) In grain boundary void growth, dislocations are emitted along the major spheroid circumference and slip away from the tip of the void, leaving multiple slip lines which sometimes can be experimentally observed (e. g., [77]).

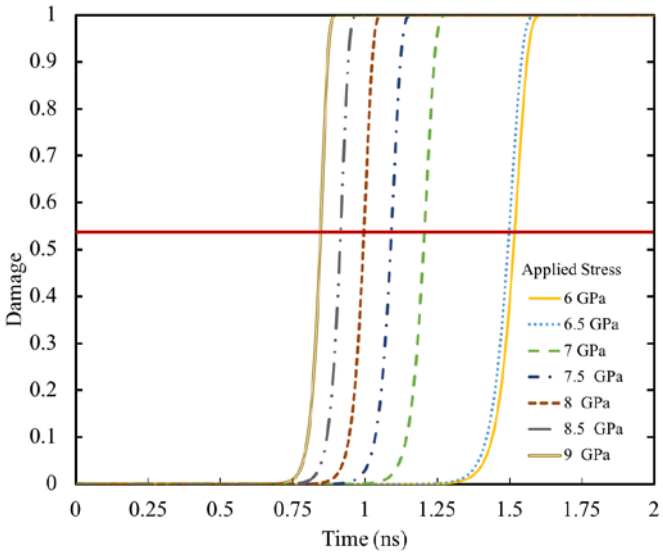

(a)

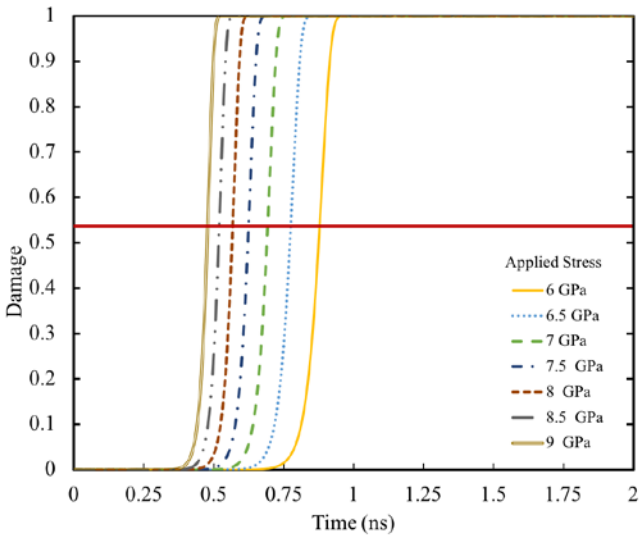

(b)

Figure 15. Predicted evolution of damage as a function of time at different tensile stress levels for (a) intragranular and (b) intergranular void nucleation and growth

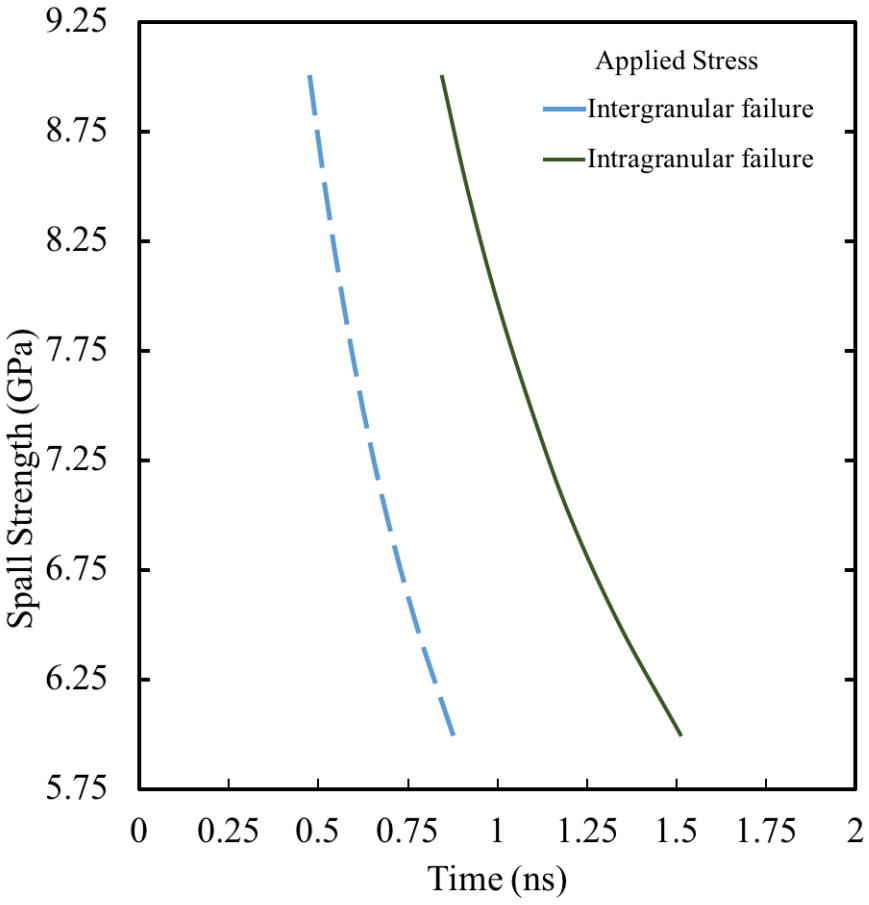

Figure 16. Spall stress (defined as D=0.5) as a function of time doe intragranular and intergranular void nucleation, growth, and coalescence. Note higher spall strength by ~2.5 GPa for monocrystalline vs. polycrystalline tantalum.